Classical Density Functional Study on Interfacial Structure and Differential Capacitance of Ionic Liquids near Charged Surfaces

Ma, Ke; Woodward, Clifford E.; Forsman, Jan

Published in:
Journal of Physical Chemistry C

2014

Classical Density Functional Study on Interfacial Structure and Differential Capacitance of Ionic Liquids near Charged Surfaces

March 20, 2014

Abstract

We designed a coarse-grained model for aromatic ionic liquids $[C_nMIM^+[Tf_2N^-]$ with cations containing different alkyl groups. Within the framework of correlation-corrected density functional theory, the interfacial structure of studied ionic liquids are compared over a range of surface charge densities, alkyl chain lengths and surface geometries. The non-polar hydrocarbon chains on cation tend to stretch out on the neutral surface. Differential capacitance of electric double layer formed by ionic liquids is explored with respect to surface electric potential. Comparison of ionic liquids model adjacent to planar, cylindrical and spherical surfaces confirms that higher and flatter differential capacitance curve is attributed to larger curvature of the surface. The influence of lengthening cation's alkyl chain on electrochemical properties is examined as well.

1 Introduction

Room-temperature ionic liquids (RTILs) are salts (usually organic) existing in the liquid state at room temperature. Potential applications of RTILs include solvents for catalysis and separation, and electrolytes in electrochemical devices.[1,2] In nearly all applications, understanding the structure-property relationship is crucial for ionic liquids both in the bulk phase and at interface. On the one hand, electrostatic coupling between cations and anions is dominant at short range, especially in the presence of a modest dielectric constant of RTILs. On the other hand, steric hindrance due to large molecular structure is quite strong and causes RTILs to remain fluid rather than to crystallize.[3] This strong interplay between steric exclusion and electrostatic interactions brings many desirable properties to RTILs including low melting point, negligible vapor pressure and high electrochemical stability. These coupled with a large variety of cations and anions to choose from, make RTILs a vigorous research area at the moment.[4,5]

Recently RTILs have been intensively studied as novel electrolyte in electric double layers (EDL) of electrical double layer capacitor (EDLCs) or supercapacitors. Differential capacitance (DC) measures the electrical energy density stored in EDLCs and varies with change of surface electrical potential.[6] The DC curve as a function of surface potential appear in bell shape, U shape (parabolic) or camel shape (i.e. a minimum at low voltages and two maxima at higher voltages in both sides), depending on factors such as RTIL structure, ion concentration, temperature and the nature of electrode. Kornyshev incorporated steric exclusion effects into mean field treatment of charged hard spheres and demonstrated the transition of DC curve from camel shape to bell shape with increasing electrolyte concentration.[6] This transition is also observed for restricted primitive model in modfied Possion- Boltzmann theory[7] and density functional theory (DFT).[8] But the

magnitude of DC among these studies is varied as a result of different solvent dielectric constant. In a more detailed RTIL model, the neutral beads are linked with forming camel shape of DC curve by facilitating rearrangements of charged beads close to electrified surface.[9] Alternating layers of cations and anions are observed near charged electrode in DFT studies by Wu et al.[10] Asymmetry in ion size and structure gives rise to asymmetry in potential dependence of DC as well according to both theoretical studies[8,9] and experiments.[11] By considering dispersion forces among RTIL particles, DC curve changes from bell shape into camel shape from simulation by Trulsson et al.[12] The nature of surface is important in affecting DC shape. Image charges are produced from strong surface polarization on metallic electrode, and will substantially enhance electrostatic screening compared with non-conducting electrode at same electrolyte profiles.[7] Meanwhile, smooth surface reports qualitatively more camel-shaped DC curve rather than bell shape.[13] Based on a density dependent effective dielectric constant in DFT, DC curve exhibits more of camel shape in comparison with the approach of fixed dielectric constant.[14] A series of studies by Feng and co-workers[15–17] confirm that DC curve becomes higher and flatter with increasing curvature in cylindrical and spherical electrodes. All findings above could be utilized for the design of more efficient electrical energy storage.

Large-scale modelling of RTILs behaviours are computationally expensive using atomistic simulations. In particular, computation on potential dependence of DC can be very inefficient for viscous RTILs, especially in confined space.[18] Mean field theories such as Poisson-Boltzmann approximation fail to account for electrostatic correlation and steric exclusion in RTILs.[3] Classical DFT offers a versatile tool to study dense electrolytes either in the bulk or near charged surface.[19–21] Previous standard classical DFT model RTILs as positive and negative charged hard spheres, and thus are rather crude in predicting structural and electrochemical properties of RTILs.

In this work, a newly developed coarse-grained model for aromatic RTILs is employed through polymer density functional treatment. The model aims to match its charge dispersion and intramolecular structure with real RTILs. While being able to model a variety of such molecules, we focus on the chemical structures of imidazolium-based RTILs: cation is the homologous series of *1-alkyl-3-methyl imidazoliums*, or $[C_nMIM^+]$ where n denotes the length of the alkyl chain. The anion will in all cases be the *bis-(trifluoromethylsulfonyl) imide*, or $[Tf_2N^-]$.

2 Models and Theory

2.1 RTIL model

Polymeric model within DFT framework has been applied to oligomeric fluids consisting of hard sphere monomers.[22,23] The coarse-grained models for both cations $[C_nMIM^+]$,$n = 2, 4, 6$ and anion $[Tf_2N^-]$ are illustrated in Figure 1. By naming cation as $[C_nMIM^+]$, the model can be easily generalized to cation with longer alkyl chain $n = 4, 6$ by sequentially adding neutral spheres to the end, with each sphere representing either CH_2 or CH_3 groups.

In an attempt to mimic its structure and charge dispersion, the imidazolium ring is modelled as a star-like structure consisting of tangentially connected spheres. The positive charge is uniformly distributed among 5 beads on or next to the imidazolium ring, where most positive charge are concentrated. The negative charge is also uniformly distributed among 5 beads, with their locations meant to represent nitrogen and oxygen atom on $[Tf_2N^-]$. This charge dispersion is aimed to be consistent with partial atom charge profiles in MD simulations.[24,25] Furthermore, all charged beads, either positive or negative, are carrying an equal amount of 0.2 elementary charge so that the total charge is one positive unit on cation and one negative unit for anion. The equal amount charge on each bead benefits handling of strong electrostatic correlation in

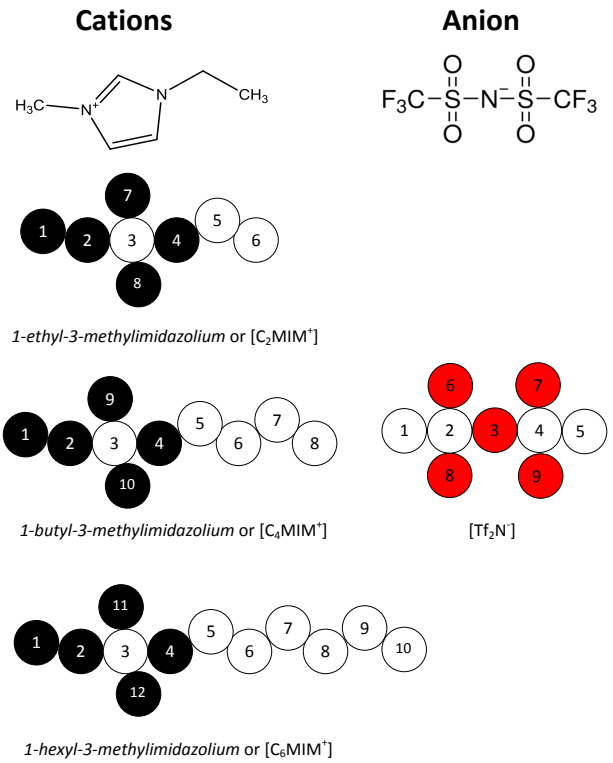

Figure 1: RTIL model of cations $[C_2MIM^+]$, $[C_4MIM^+]$ and $[C_6MIM^+]$; anion $[Tf_2N^-]$. Coloured spheres are charged ones while the rest are neutral ones.

RTILs as discussed later.

As neutral groups in RTILs are explicitly considered in this model and charges are dispersed to imitate real charge profiles, the only missing polarization is then electronic polarization of each bead on cation and anion. For coulomb potential bewteen charged beads in the model, dielectric constant ϵ_r is set equal to that of benzene, i.e. $\epsilon_r = 2.3$, which reflects average electronic polarizability in system space occupied by studied RTILs. All beads have a same diameter of $\sigma = 2.4$ Å as in first development of this model.[26]

Overall, all species of beads are modelled as hard spheres at short range less than one bond diameter, and are also interacting with an pairwise Lennard-Jones potential beyond one bond diameter. Regarding electrostatic interactions, an "coulomb hole" version of electrostatic correlation is employed as correction for mean-field theory. All these interactions will be discussed on a term by terms basis. Our hope is to achieve qualitatively good agreemen ostatic properties.

2.2 Polymer density functional theory

In polymer DFT applied for ionic liquids, each bead on RTIL model is viewed as one monomer of polymeric cation and anion. Total free energy is then expressed as a functional of monomer densities of all kinds on the polymer.[27,28] Total monomer densities are derived by integrating polymer density over all configurations. Density of every kind of monomer is allowed to fluctuate to maintain equilibrium with the bulk reservoir. By minimizing the free energy functional with respect to the monomer densities, equilibrium properties of RTILs are obtained.[29]

The grand potential functional Ω is related to Helmholtz energy via Legendre transform,

$$\begin{aligned}\Omega = F^{id}[N_c(\mathbf{R}), N_a(\mathbf{R})] + F_{hs}[\bar{n}_s(r)] + F_{disp}[n_s(r), n_s(r')] + F_{corr}[n_\alpha(r), n_\lambda(r')] \\ + F^{el}_{surf}[n_\alpha(r), n_\lambda(r')] + F^{disp}_{surf}[n_s(r)] - \sum_i (\mu_i + q_i \Psi_D) n_i(r)\end{aligned} \tag{1}$$

where $N_a(\mathbf{R}), N_c(\mathbf{R})$ are the set of polymeric densities describing all species on anion and cation, here $\mathbf{R}$ represents the sites of all constituent spheres on either anion or cation. Similarly, as $\alpha, \lambda = a$, $n_a(r)$ is density of negative sphere; as $\alpha, \lambda = c$, $n_c(r)$ for positive sphere density, here r represent the site of single sphere. Therefore

$$n_\alpha(r) = \int d\mathbf{R} \sum_i \delta(r - r_i) N(\mathbf{R}) \tag{2}$$

where $\delta(r)$ is a Dirac delta function; i runs over all species in the model and the sum is over all configurations of polymer; $\{n_\alpha(r); \alpha = a, c, n, s\}$ are the charge site densities of positive, negative, neutral and all beads, so $n_s(r) = n_c(r) + n_a(r) + n_n(r)$.

In grand potential expression, μ_i is chemical potential of speicies i in the bulk; q_i is charge on species i; Ψ_D represents donnan potential which will make sure the whole system is electroneutral.

Helmholtz free energy is then written as a sum of ideal and all other types of excess contributions.

2.2.1 Ideal chain term

The contribution to free energy due to ideal chain is described by:

$$F^{id}[N_c(\mathbf{R}), N_a(\mathbf{R})] = \sum_{\alpha=a,c} \int N_\alpha(\mathbf{R}) \left(\ln[N_\alpha(\mathbf{R})] - 1\right) d\mathbf{R} + \sum_{\alpha=a,c} \int N_\alpha(\mathbf{R}) (V^{(B)}_\alpha(\mathbf{R}) + V^{ex}_\alpha(\mathbf{R})) d\mathbf{R} \tag{3}$$

where $V^{(B)}_\alpha(\mathbf{R})$ is the bonding energy and $V^{ex}_\alpha(\mathbf{R})$ is the external force field

2.2.2 Hard sphere term

Excluded volume effect describes steric exclusion at short separation between all species of hard sphere monomers. This effect is represented by the hard sphere term $F_{hs}[\bar{n}_s(r)]$ applied to hard sphere chain. In generalized van der Waals theory for simple hard spheres,[30] the weighted density is an average over total monomer density within one bond diameter, given by

$$\bar{n}_s(r) = \frac{3}{4\pi\sigma^3} \int_{|r-r'|<\sigma} n_s(r') dr'. \tag{4}$$

Derived from Generalized Flory-Dimer equation of state, $F_{hs}[\bar{n}_s(r)]$ is a highly non-linear term of weighted density. This hard sphere term for excluded volume interaction has been proved accurate in reproducing non-uniform structures for hard core polymer model.[27,31]

2.2.3 Non-bonded non-electrostatic interaction

All monomers, both charged and neutral, interact with each other via a pairwise additive Lennard-Jones potential, corresponding to the non-bonded non-electrostatic interaction in molecular simulations. Its contribution to free energy equals the integral of L-J potential over all monomers,

$$F_{disp}[n_s(r), n_s(r')] = \frac{1}{2} \int \int_{|r-r'|) \geq \mathbf{oe}} n_s(r) n_s(r') \phi_{LJ}(|r - r'|) dr \tag{5}$$

where

$$\phi_{LJ}(r) = 4\epsilon_{LJ}[(\frac{\sigma}{r})^{12} - (\frac{\sigma}{r})^{6}] \tag{6}$$

Here r is the separation between monomer centres; Attractive strength and repulsive range of the non-electrostatic interaction are determined by $\epsilon_{LJ} = 100k_BK$ and $\sigma = 2.4$Å. These two parameters are in line with the earlier study [26] which reproduced bulk density of pure L-J fluids in MD simulations. Repulsive part of Lennard-Jones potential is included to compensate for the missing stiffness in density functional treatment of polymeric chains. Those stiffness are taken into account in simulations whereby particles are unable to get too close due to constraint in dihedral and torsional angle.

2.2.4 Electrostatic Correlations

Mean field theories overestimate electrostatic interaction by allowing complete penetration of other ions (both like charges and opposite charges) into its own hard sphere exclusion hole. Electrostatic correlation term is introduced by removal of "coulomb hole" on top of mean field coulomb interaction. Then correlation between like charges should be less repulsive than coulomb potential while correlation between oppostive charges should be less attractive than coulomb potential. In principle, electrostatic correlation contributes to the excess free energy functional by second-order term of relevant particle densities, i.e.

$$F_{corr} \approx \frac{1}{2}\int\int n_\alpha(r)n_\lambda(r')K_{corr}^{\alpha\lambda}(|r-r'|)drdr' = F_{el}^{like} + F_{el}^{unlike} \tag{7}$$

The algebraic form of the overall *correlation kernels*, $K_{corr}^{\alpha\lambda}$, is different when α and λ stand for like or opposite charges.

As particles carrying charges of the same sign naturally tend to avoid each other, overall *like-like* Coulombic interactions is then given by

$$F_{el}^{like} = \frac{1}{2}\int\int \sum_{\alpha=a,c} n_\alpha(r)n_\alpha(r')H_\alpha(|r-r'|)\Phi_{el}^{\alpha\alpha}(|r-r'|)drdr' \tag{8}$$

whereby an exponential "coulomb hole" is proposed, i.e.,

$$H_\alpha(r) = (1 - e^{-\lambda_\alpha r}) \tag{9}$$

The parameter λ_α is determined with bulk ion concentration such that the "coulomb hole" function fits exclusion in the bulk to one single ion,

$$n_\alpha^{(b)}\int dr\{H_\alpha(|r|) - 1\} = -1 \tag{10}$$

where $n_\alpha^{(b)}$ is the bulk density of the species α. Thus we obtain,

$$\lambda_\alpha = \frac{\sqrt{2}}{s_\alpha} \tag{11}$$

with

$$s_\alpha = \left[\frac{3}{4\pi n_\alpha^b}\right]^{1/3} \tag{12}$$

At the same time, a hard sphere "coulomb hole" with adjustable size is proposed for correlations between opposite charges. The overall *unlike* Coulombic interactions between anions and cations becomes

$$F_{el}^{unlike} = \frac{1}{2}\int\int \sum_{\alpha\neq\beta} n_\alpha(r) n_\beta(r') \Theta(|r-r'| - d_{\alpha\beta}) \Phi_{el}^{\alpha\beta}(|r-r'|) dr dr' \tag{13}$$

where the Heaviside function is defined as: $\Theta(x) = 1$ for $x > 0$ and $\Theta(x) = 0$ for $x \leq 0$. By setting $d_{\alpha\beta} = \chi\sigma_{\alpha\beta}$, χ is chosen so as to obtain same bulk density in DFT as in simulations under ambient pressure and temperature.[26] For $[C_nMIM^+][Tf_2N^-]$ model in this work, the values are $\chi = 0.82, 0.84$ and 0.84 for $n = 2, 4, 6$ respectively. The "coulomb hole" method for electorstatic correlation has succeeded in predicting interfacial structure compared with simulation results.[26,32]

2.2.5 Surface charge interaction

Surface charge interact with both itself and RTILs charge via mean field coulomb potential (Eq.15), given by following expressions

$$F_{surf}^{el}[n_\alpha(r), n_\lambda(r')] = \int \sum_\alpha V_{el}(r) n_\alpha(r) dr + E_{surf} \tag{14}$$

and

$$\phi_{el}^{\alpha\lambda}(r) = \frac{z_\alpha z_\lambda e^2}{4\pi\epsilon_0\epsilon_r r} \tag{15}$$

where z_α and z_λ are the valencies of the interacting pair of ion, e is the elementary charge, $\epsilon_r = 2.3$ as discussed already and ϵ_0 is vacuum permittivity. The quantity $V_{el}(r)$ is electrical potential due to electrode charges, and E_{surf} represents the mutual interactions of surface charges. Surface charges are uniformly smeared out on the plane located at center of carbon atom for all three geometries of surface, with inverse surface charge density denoted by a_s. Image charge effects are not considered in this work and target simulations.[17,33]

2.2.6 Surface non-electrostatic interaction

To match the surface conditions in simulation,[33] DFT models electrode as a single sheet of graphene in planar, cylindrical and spherical shapes respectively. The surface is composed of uniform distribution of carbon atoms with a density of roughly 2 atom per σ^2, i.e. $\rho_s = 2$, a typical value for a unit hexagonal cell of graphene. Non-electrostatic interaction between surface atom and each bead in RTILs model is same type of Lennard-Jonnes potential between RTIL beads. To make a comparison, we plot non-electrostatic interaction between *Ccn i.e. sp2 carbon atom* in UA/EA model of the simulation.[24] In particular, that potential crosses zero at around 3.6Å and its depth of potential well is around $0.1kT$, similar to parameters in many force fields of graphene surface. We then find these parameters comparable with DFT parameters. Because DFT adopts the coarse-grained model in which bead bead L-J potential is supposed to be rewritten into a large magnitude and at a larger distance ($\sigma_w = 3.6$Å) than atomistic simulations. Non-electrostatic interaction between the whole surface and all type of beads is obtained by integrating the Lennard-Jones potential (Eq.6) over the surface.

For infinitely large planar surface the expression is

$$\omega_{PLJ}(z) = 4\pi\epsilon_{LJ}\rho_s \left[\frac{1}{5}(\frac{\sigma_w}{z})^{10} - \frac{1}{2}(\frac{\sigma_w}{z})^4\right] \tag{16}$$

where z is the distance from the center of surface atom.

For infinitely long cylindrical surface with radius $r_0 = 6.8$Å, potential as a function of distance from cylindrical surface is given by

$$\omega_{CLJ}(z) = 4\epsilon_{LJ} \int_{-\infty}^{+\infty} \int_{0}^{2\pi} \left[(\frac{\sigma_w}{\rho})^{12} - (\frac{\sigma_w}{\rho})^{6} \right] d\theta dx \tag{17}$$

where

$$\rho = \sqrt{2r_0(r_0 + z)(1 - cos(\theta)) + z^2} \tag{18}$$

Unfortunately, analytical solution is not available and it must be solved numerically instead. The numerical solution is saved into vectors in DFT program and thus won't compromise the efficiency of DFT calculation.

For spherical surface with radius $r_0 = 7.1$Å, integrate the L-J potential over the spherical surface and we get

$$\omega_{SLJ}(z) = \frac{4\pi\epsilon_{LJ}\rho_s r_0}{(r_0 + z)} \left\{ \frac{\sigma_w^4}{2} [\frac{1}{(z + r_0)^4} - \frac{1}{(z - r_0)^4}] - \frac{\sigma_w^{10}}{5} [\frac{1}{(z + r_0)^{10}} - \frac{1}{(z - r_0)^{10}}] \right\} \tag{19}$$

Comparison of 3 geometries shows almost identical non-electrostatic potential with respect to distance from the surface (Fig. 2). The minor difference is that planar graphene surface exhibts a deeper potential well than cylindrical surface than spherical one.

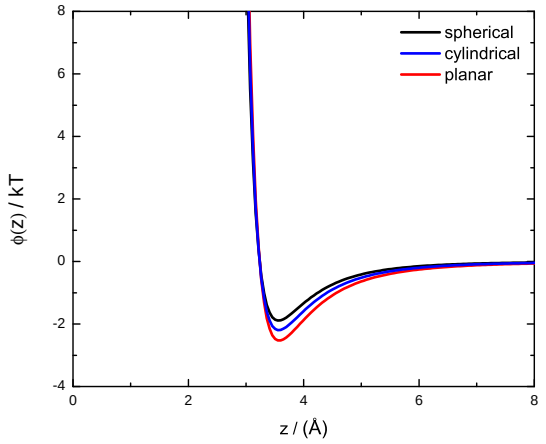

Figure 2: Non-electrostatic potential comparison for planar, cylindrical and spherical graphene surfaces.

So the whole system will display variant densities along the surface normal direction and symmetric structure in other 2 directions. Innovations in DFT approach here lie in integrating all type of required interaction functions (e.g. Lennard-Jones potential, correlation-corrected coulombic interaction) between different spherical shells constituting the spherical surface system. While for cylindrical electrode, analytical solutions is unavailable for most of interaction functions. So the solution need be derived numerically to make sure DFT remains versatile under circumstances of special geometry. After procedure of numerous iterations, the system will reach equilibrium with densities of all species converging to bulk value at the boundary.

3 Results

3.1 Interfacial structure

We first explored interfaical structure of RTILs using our coarse-grained model adjacent to neutral planar surface. Positive, negative, neutral and total beads densities are respectively examined as a function of distance from surface for $[C_2MIM^+][Tf_2N^-]$ in Figure 3. Neutral

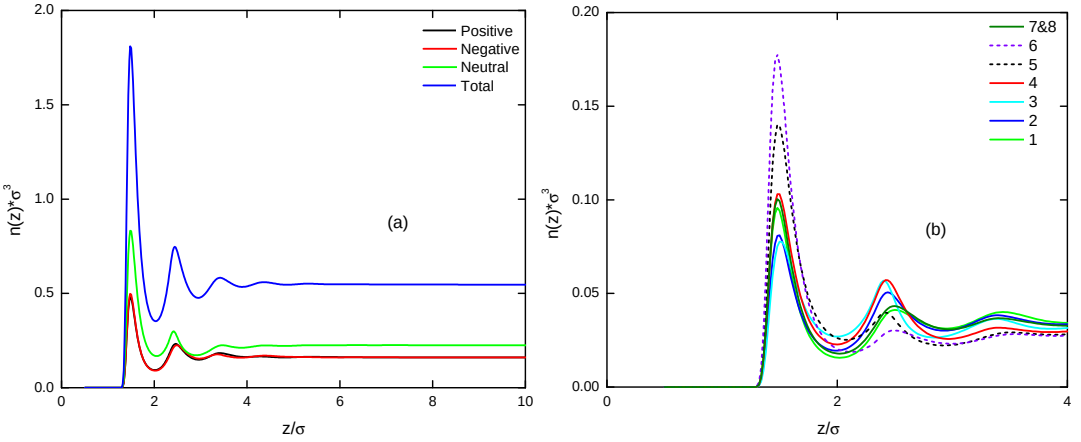

Figure 3: Density profiles in $[C_2MIM^+][Tf_2N^-]$ near planar neutral surfaces for (a) positive, negative, neutrla and total beads (b) each single beads on cation $[C_2MIM^+]$. Alkyl chain is composed of dashed bead 5 and 6. Bead number is shown in Figure 1.

spheres are found to have stronger adsorption than both positive and negative beads. From the perspective of single bead density for all species on cation (Fig. 3(b)), end bead of alkyl chain has strongest adsorption. Its neighbouring -CH_2 bead has second highest density rather than all other beads on imidazolium. This suggests that it's energetically favorable for alkyl chain of cation to stretch out on the surface.[34]

The structured cation profile is more obvious for $[C_6MIM^+][Tf_2N^-]$ with a longer alkyl chain. As is in Figure 4(b), end bead has an even stronger adsorption than in $[C_2MIM^+]$, suggesting a stronger coordination with larger neutral part. While going from end bead to central imiazolium bead, the adsorption decreases gradually.

Then densities of positive and negative bead in $[C_2MIM^+][Tf_2N^-]$ are explored at a range of surface charge densities. In the presence of charged surface, alternating cations and anion layers are observed as shown in Figure 5.

Typical width of each layer is of the order of one bead diameter. Overscreening take place as the first layer delivers more charges of counter-ion than surface charge. The first counter-ion peak grows as surface charge density increases, indicating a more structured profiles along the distribution.

Unlike the center of mass density studied in MD simulations,[35] a weaker second peak for counter-ion exist in DFT's charged bead density (Fig. 5). It's understandable that some charged groups of counter- ion are indeed pushed away to second layer but won't be counted in center of mass density. Regardless of what the surface charge density is, densities of all species converge to bulk value at large distance, acting as evidence for system equilibrium

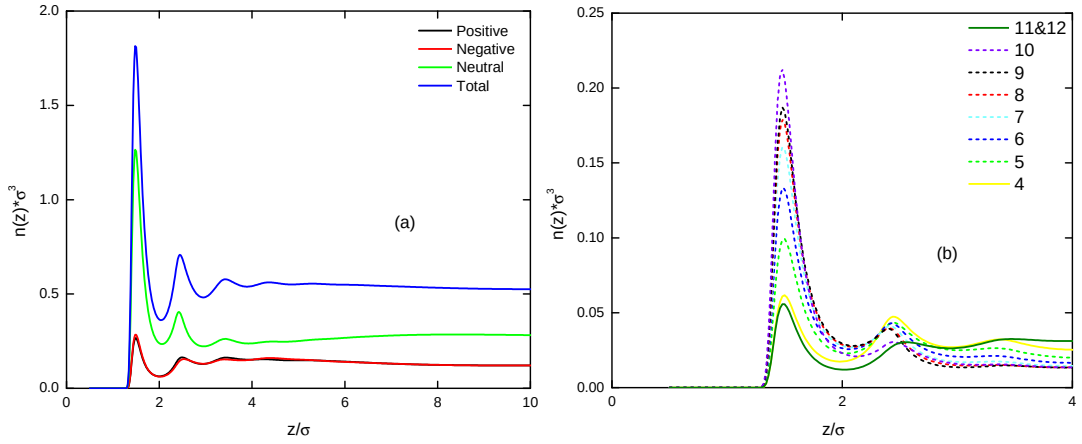

Figure 4: Density profiles in $[C_6MIM^+][Tf_2N^-]$ near planar neutral surfaces for (a) positive, negative, neutrla and total beads (b) each single beads on cation $[C_6MIM^+]$. Alkyl chain is from dashed bead 5 to 10. Bead number is shown in Figure 1.

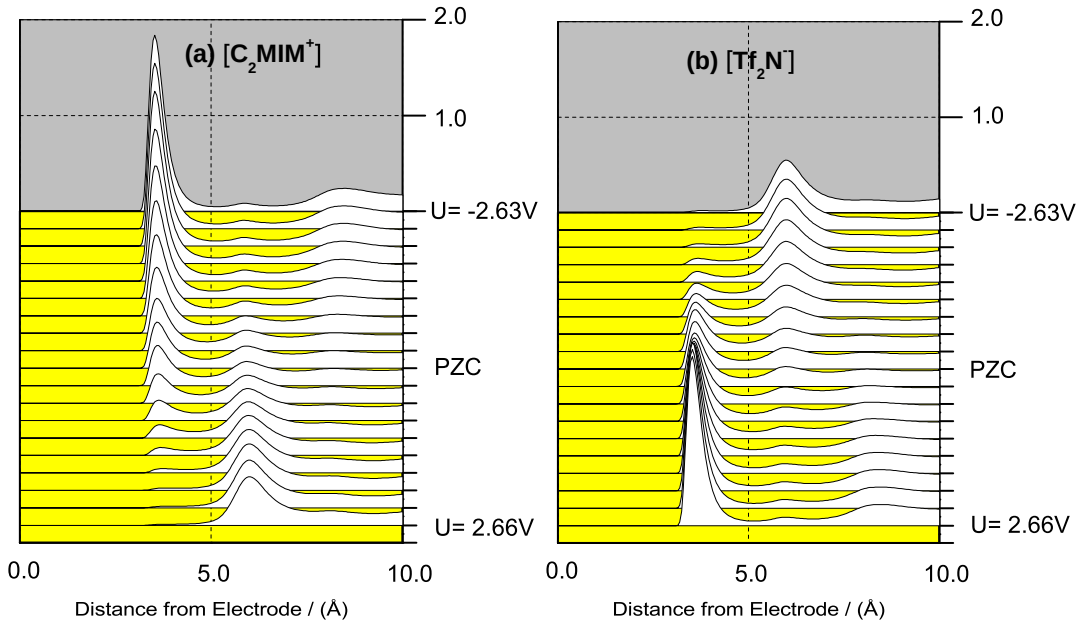

Figure 5: Density profiles of (a) positive spheres and (b) negative spheres in $[C_2MIM^+][Tf_2N^-]$ model near planar surface across different surface electrical potentials

3.2 Differential capacitance

Differential capacitance per unit area is defined as the derivative of surface charge density with respect to electrical potential at surface. DC curve undergoes a transition from camel shape to bell shape, or the other way around based on the competition between electrostatic attraction and steric exclusion at region close to electrode. The widely seen camel-shaped DC curve results

in growing overscreening at low voltages and dominating crowding effect at high voltages. For our $[C_2MIM^+][Tf_2N^-]$ model, however, overscreening regime begins to be suppressed by RTILs saturation from neutral surface. pointed out in MD simulations,[36] RTIL's high affinity to neutral graphite surface reaches saturation limit of total bead adsorption. As a result, DC curve exhibits bell shape with a maximum near potential of zero charge (PZC) in Figure 6. This finding

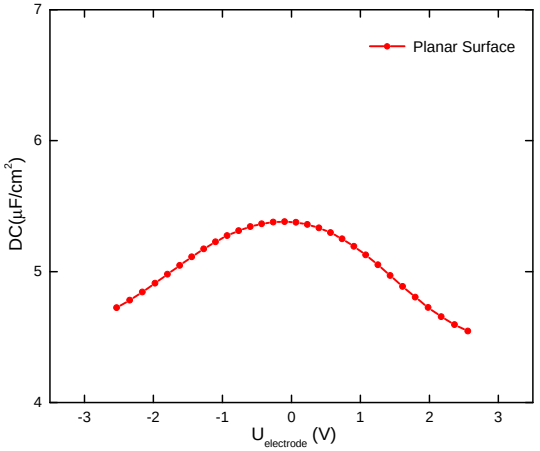

Figure 6: Differential capacitance of $[C_2MIM^+][Tf_2N^-]$ as function of surface electrical potential near planar surface

is essentially consistent with simulations[12] which proved average depletion at the surface is relevant with the minimum of DC at around PZC and adsorption relevant iwth maximum. As surface charge density rises, counter-ion dominates the microstructure in closest layer to surface. But counter-ion concentration doesn't increase as rapid as surface charges in both positive and negative side (Fig. 5). Therefore, DC curve shows the trend of saturation of screening at large voltages.

3.2.1 Curvature effect

The relevance surface geometry has with differential capacitance is studied by comparing RTILs properties near planar, cylindrical and spherical surfaces. First, structural comparison is conducted for the same RTIL $[C_2MIM^+][Tf_2N^-]$ near different surfaces at same surface charge density in Figure 7(a),(b),(c). Apparently first counter-ion peak near planar surface is higher than cylindrical surface than spherical surface. However, the order is opposite among the 3 surfaces when the question becomes in which case overscreening is strongest.

To further understand phenomenon, we employ screening factor to evaluate overscreening at different surface geometries. Screening factor is defined as the minus of ratio of electrolyte charges within certain distance from surface over over surface charge.[16,33] Its dependence on curvature rises from planar surface (Eq.20) to cylindrical (Eq.21) and spherical surface (Eq.22).

$$C_f(d) = -\frac{\int_0^d \rho(z)dz}{\sigma_s} \tag{20}$$

$$C_f(d) = -\frac{\int_{r_0}^{r_0+d} \rho(z)\frac{z}{r_0}dz}{\sigma_s} \tag{21}$$

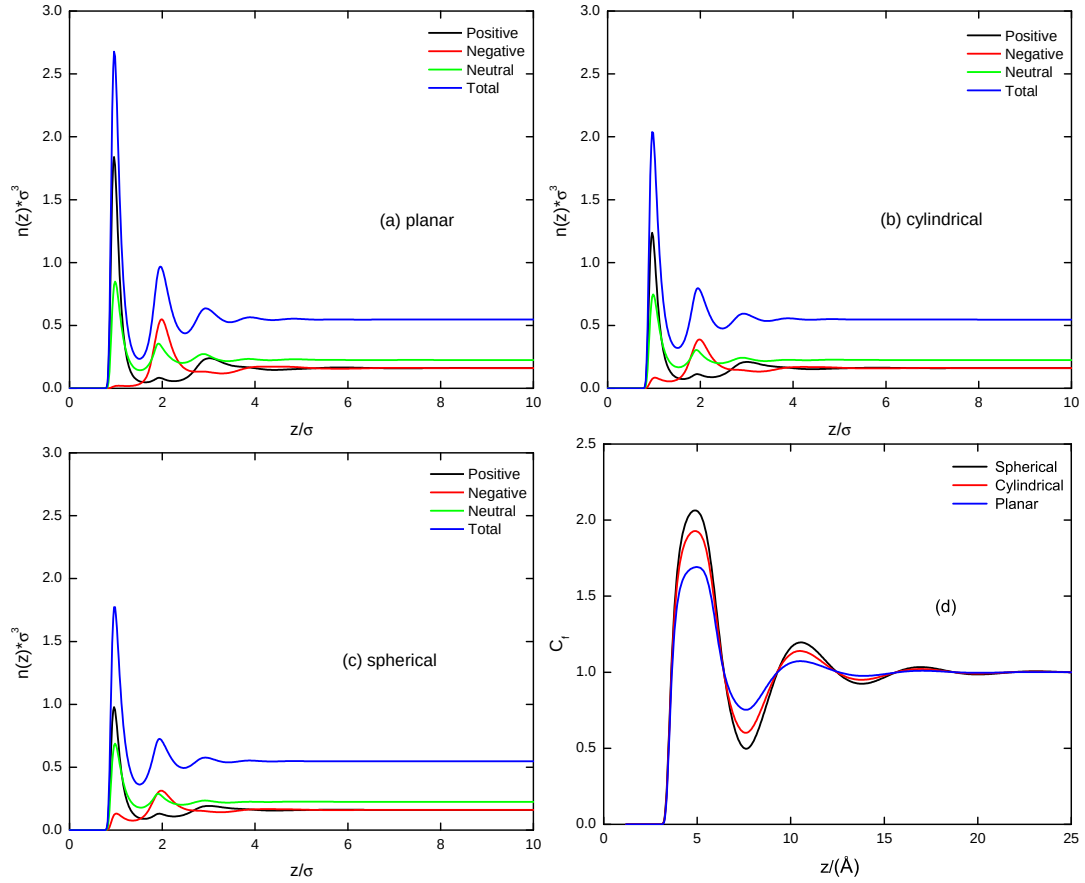

Figure 7: Density profiles of positive, negative, neutral and total beads of $[C_2MIM^+][Tf_2N^-]$ near (a)planar, (b)cylindrical, (c)spherical surfaces with charge density $-120\text{Å}^2/e$; (d) screening factor comparison of $[C_2MIM^+][Tf_2N^-]$ at 3 different surfaces with charge density $-120\text{Å}^{\ 2}/e$

$$C_f(d) = -\frac{\int_{r_0}^{r_0+d} \rho(z)\frac{z^2}{r_0^2}dz}{\sigma_s} \tag{22}$$

For a more curved electrode, per unit area on electrode surface corresponds to larger space in the system available for screening electrode charges. Curvature effect is then fully embodied in that at same surface charge density, counter-ions near planar surface builds highest first peak while planar surface is least screened by electrolytes among 3 surfaces based on screening factor in Figure 7.

In MD simulations of both polarizable or non- polarizable model, partial atom charges are considered explicitly so that only vacuum permittivity ϵ_0 enters coulomb potential. That is different from DFT which has a more coarse-grained charge distribution and must employ dielectric constant ϵ_r to account for electronic polarization. This being said, oscillation of charge density obtained from DFT is equivalent to screened version of real charge density in simulations by a factor of dielectric constant. That's why we see a less drastic screening curve in Figure 7 (d) than simulations.[33]

Figure 8 displays complete comparison of DC curve as a function of surface potential near

planar, cylindrical and spherical surfaces. Here DC is normalized to per unit area on the surface.

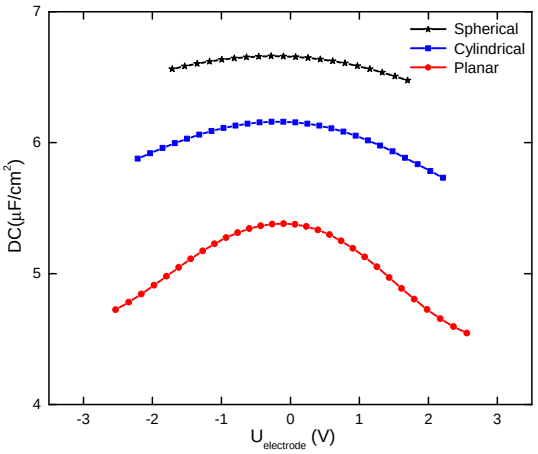

Figure 8: Differential capacitance of $[C_2MIM^+][Tf_2N^-]$ near planar, cylindrical and spherical surfaces

The major principle is that the larger curvature the surface owns, the high and flatter DC curve is obtained. This trend qualitatively agrees with MD simulations.[16,17,33] we focused on. The enhanced screening effect can be explained in the first place, by a lower potential drop across more curved space of EDL at same surface charge density. Additionally, larger curvature brings larger space which makes counter-ion screen electrode stronger and less likely to saturate.

3.2.2 Ion size effect

Ion size and structure play an important role in interfacial strucures from the perspective of excluded volume effect. Figure 9 gives a comparison of DC curves with different alkyl chain on cation. In general longer hydrocarbon chain on cation means a lower bulk density of RTIL, and a

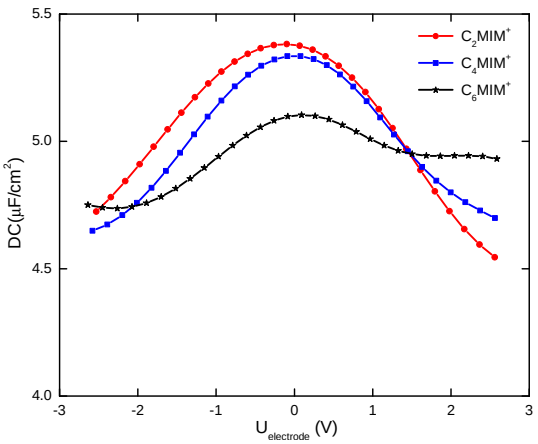

Figure 9: Differential capacitance of $[C_2MIM^+][Tf_2N^-]$, $[C_4MIM^+][Tf_2N^-]$,$[C_6MIM^+][Tf_2N^-]$ near planar surfaces

lower DC magnitude as well especially at large voltages. Our data from the coarse-grained model confirms a decreasing DC level by increasing alkyl chain length near negative surface (Fig.9). For $[C_2MIM^+][Tf_2N^-]$, quite symmetric DC curve is attributed to similar size of caiton and anion. As alkyl chain grows from $n = 2$ to $n = 6$, DC curve is found more asymmetric between positive and negative side. Specifically, DC of $[C_6MIM^+][Tf_2N^-]$ remains relatively flat at large positive potentials.

To better explore DC curve, we compare the potential dependence of screening factor for 3 types of RTILs in our model. For all 3 types of RTILs, first peak of screening factor always gets

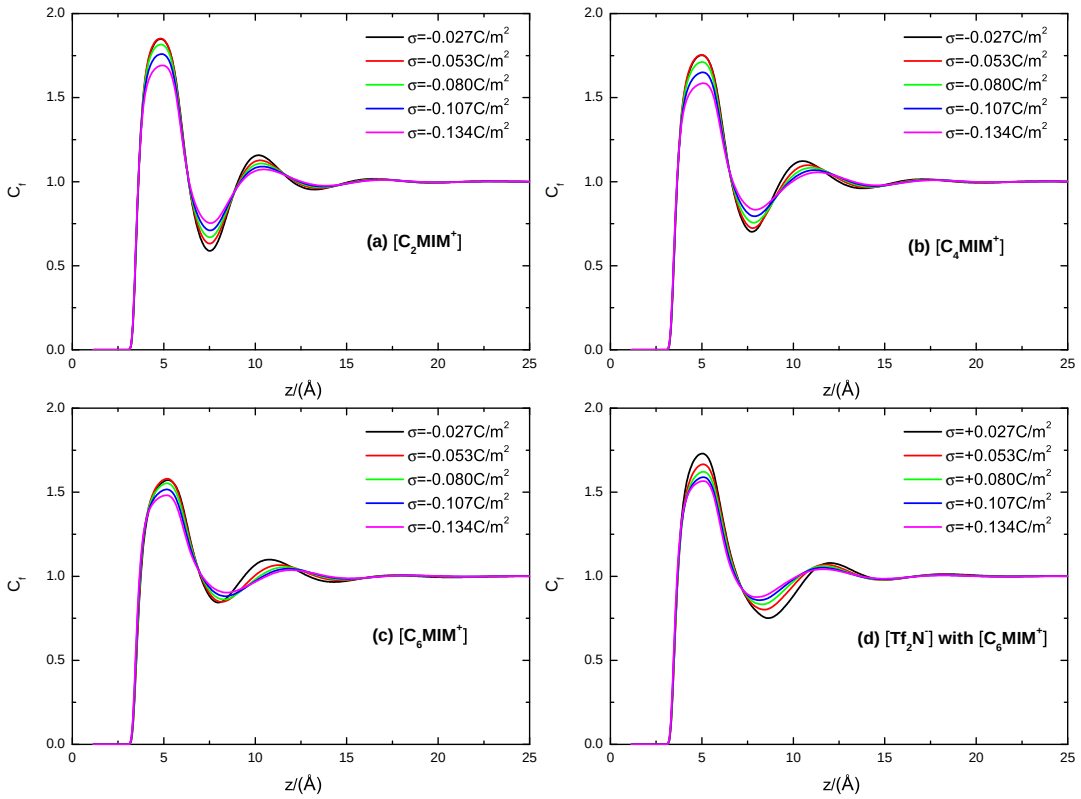

Figure 10: Comparison of screening factor as a function of distance from planar surface with different charge densities for (a)$[C_2MIM^+][Tf_2N^-]$ near negative surface (b) $[C_4MIM^+][Tf_2N^-]$ near negative surface (c)$[C_6MIM^+][Tf_2N^-]$ near negative surface (d) $[C_6MIM^+][Tf_2N^-]$ near positive surface

lower with increasing surface charge density (Fig. 10). This agrees well with the trend of reduced overscreening due to stronger crowding in EDL. At the same time, the peak of screening factor is generally higher for cations with shorter alkyl chains, corresponding to higher DC curve in negative side of Figure 9.

In particular, the role played by added $-CH_2 - CH_3$ group is revealed for screening factor of cation (Fig.10(c)) and anion (Fig.10(d)) in $[C_6MIM^+][Tf_2N^-]$. As shown in Figure 10(c), the first valley and second peak of screening factor is shifted futher away from surface as surface charges increases. After comparing with $[C_2MIM^+][Tf_2N^-]$ (Fig. 10(a)) and $[C_4MIM^+][Tf_2N^-]$ (Fig.10(d)), this shift is attributed to added $-CH_2 - CH_3$ on first peak's $[C_6MIM^+]$ which pushes following anion or cation away. In a similar mechanism, the second

valley in Figure 10(d), formed by larger cation density, becomes shallower and moves closer to increasingly positive surface. The rapidly diminishing co-ion concentration at second layer keeps overall screening strong over a large potential range. Then this structural behaviour helps explain a rather flat DC curve at large positive potential for $[C_6MIM^+][Tf_2N^-]$ in Figure 9.

Meanwhile, it is indeed discovered in simulation that DC remain flat or even increases with increasing potential at large voltages.[36] The usual scenario that DC curve up at large potential is associated with the mechanism of how RTILs with longer alkyl chain is capable of reorganizing its structures in response to surface charge increase. MD simulations have addressed the unique potential influence on DC curve through analysis of cumulative density of specific groups and atoms in RTILs.[35]

4 Conclusions and Outlook

A coarse-grained model has been adopted for aromatic RTILs with density functional treatment. Parameters in the model are chosen under the guide of simulation force field of the same RTILs. DFT results achieved qualitative agreement with simulation near electrodes of different geometries. Curvature effect is confirmed by the distinction in DC curve among planar, cylindrical and spherical surfaces. Differences in cation and anion structure give rise to subtle changes in interfacial structure and electrochemical properties. The impact of various factors on DC curve can always be rationalized by interpreting the competition between electrostatic attraction from surface charge and steric repulsion from RTILs. In conclusion, the approach in this work allows intensive studies of quantities and behaviours that are inefficient with simulations, such as differential capacitance, and interfacial structures of special geometries. We notice that for the same type of ionic liquids, Vatamanu et al[35] observed camel-shaped DC curve instead of bell shape presented in this work and simulations.[33] The discrepancy is believed to be mainly caused by neglect of image charges in latter studies. In the future, we hope to explore image charge's effect on electric double layer structures and differential capacitance of RTILs.

References

[1] H. Weingartner, *Angew Chem Int Ed Engl*, 2008, **47**, 654–70.

[2] R. Rogers and K. Seddon, *Ionic Liquids, Industrial Applications to Green Chemistry, ACS Symp. Series 818*, Am. Chem. Soc., Washington, 2002.

[3] J. Forsman, C. E. Woodward and M. Trulsson, *J Phys Chem B*, 2011, **115**, 4606–12.

[4] R. Hagiwara and Y. Ito, *Journal of Fluorine Chemistry*, 2000, **105**, 221 – 227.

[5] F. Maier, T. Cremer, C. Kolbeck, K. R. J. Lovelock, N. Paape, P. S. Schulz, P. Wasserscheidc and H. P. Steinruck, *Physical Chemistry Chemical Physics*, 2010, **12**, 1905–1915.

[6] A. A. Kornyshev, *Journal of Physical Chemistry B*, 2007, **111**, 5545–5557.

[7] C. W. Outhwaite, S. Lamperski and L. B. Bhuiyan, *Molecular Physics*, 2011, **109**, 21–26.

[8] D.-e. Jiang, D. Meng and J. Wu, *Chemical Physics Letters*, 2011, **504**, 153–158.

[9] N. Georgi, A. A. Kornyshev and M. V. Fedorov, *Journal of Electroanalytical Chemistry*, 2010, **649**, 261–267.

[10] J. Z. Wu, T. Jiang, D. E. Jiang, Z. H. Jin and D. Henderson, *Soft Matter*, 2011, **7**, 11222–11231.

[11] V. Lockett, R. Sedev, J. Ralston, M. Horne and T. Rodopoulos, *Journal of Physical Chemistry C*, 2008, **112**, 7486–7495.

[12] M. Trulsson, J. Algotsson, J. Forsman and C. E. Woodward, *Journal of Physical Chemistry Letters*, 2010, **1**, 1191–1195.

[13] J. Vatamanu, L. Cao, O. Borodin, D. Bedrov and G. D. Smith, *The Journal of Physical Chemistry Letters*, 2011, **2**, 2267–2272.

[14] Y. Lauw, M. Horne, T. Rodopoulos and F. Leermakers, *Physical Review Letters*, 2009, **103**, year.

[15] G. Feng, R. Qiao, J. Huang, S. Dai, B. G. Sumpter and V. Meunier, *Phys Chem Chem Phys*, 2011, **13**, 1152–61.

[16] G. Feng, D.-e. Jiang and P. T. Cummings, *Journal of Chemical Theory and Computation*, 2012, **8**, 1058–1063.

[17] G. Feng, S. Li, J. S. Atchison, V. Presser and P. T. Cummings, *The Journal of Physical Chemistry C*, 2013, **117**, 9178–9186.

[18] R. Szparaga, C. E. Woodward and J. Forsman, *The Journal of Physical Chemistry C*, 2013, **117**, 1728–1734.

[19] C. E. Woodward, *The Journal of Chemical Physics*, 1991, **94**, 3183.

[20] J. Wu, *AIChE Journal*, 2006, **52**, 1169–1193.

[21] R. Szparaga, C. E. Woodward and J. Forsman, *The Journal of Physical Chemistry C*, 2012, **116**, 15946–15951.

[22] C. E. Woodward and J. Forsman, *J Chem Phys*, 2008, **129**, 054902.

[23] Z. D. Li and J. Z. Wu, *Journal of Physical Chemistry B*, 2006, **110**, 7473–7484.

[24] O. Borodin, *Journal of Physical Chemistry B*, 2009, **113**, 11463–11478.

[25] G. E. Logothetit, J. Ramos and I. G. Economou, *Journal of Physical Chemistry B*, 2009, **113**, 7211–7224.

[26] Turesson, R. Szparaga, K. Ma, C. E. Woodward and J. Forsman, *Soft Matter*, 2014, –.

[27] J. Forsman and C. E. Woodward, *J Chem Phys*, 2004, **120**, 506–10.

[28] Z. Li, D. Cao and J. Wu, *J Chem Phys*, 2005, **122**, 174708.

[29] J. Forsman, R. Szparaga, S. Nordholm, C. E. Woodward and R. Penfold, *Ionic Liquids - Classes and Properties*, InTech, Rijeka, 2011, pp. 127–150.

[30] S. Nordholm, M. Johnson and B. C. Freasier, *Australian Journal of Chemistry*, 1980, **33**, 2139–2150.

[31] C. E. Woodward and A. Yethiraj, *The Journal of Chemical Physics*, 1994, **100**, 3181.

[32] J. Forsman and S. Nordholm, *Langmuir*, 2012, **28**, 4069–79.

[33] G. Feng, S. Li, V. Presser and P. T. Cummings, *The Journal of Physical Chemistry Letters*, 2013, **4**, 3367–3376.

[34] S. Wang, S. Li, Z. Cao and T. Y. Yan, *Journal of Physical Chemistry C*, 2010, **114**, 990–995.

[35] J. Vatamanu, O. Borodin, D. Bedrov and G. D. Smith, *The Journal of Physical Chemistry C*, 2012, **116**, 7940–7951.

[36] Z. Hu, J. Vatamanu, O. Borodin and D. Bedrov, *Physical Chemistry Chemical Physics*, 2013, **15**, 14234.